Permeability and elastic properties of rocks from the northern Hikurangi margin: Implications for slow-slip events

Nicola Tisato[1], Carolyn D. Bland[1*], Harm Van Avendonk[2], Nathan Bangs[2], Hector Garza[1], Omar Alamoudi[1], Kelly Olsen[2†], Andrew Gase[2‡]

[1] Department of Earth and Planetary Sciences, Jackson School of Geosciences, The University of Texas at Austin, Austin, TX, U.S.

[2] Institute for Geophysics, Jackson School of Geosciences, The University of Texas at Austin, Austin, TX, U.S.

[*] Now at: Pariveda Solutions, Dallas, TX, U.S.

[†] Now at: Descartes Labs, 1607 Paseo de Peralta, Suite B, Sante Fe, NM, U.S.

[‡] Now at: Geology Department, Western Washington University, Bellingham, WA, U.S.

Corresponding author: Nicola Tisato (nicola.tisato@jsg.utexas.edu)

Key Points:

- Elastic properties, plastic deformation, and permeability of northern Hikurangi margin rocks
- Permeability-porosity relationship in accretionary prisms
- Clay swelling and plastic deformation controls permeability healing, providing a mechanism justifying slow-slip event cyclicity

Abstract

Fluid flow and pore-pressure cycling are believed to control slow slip events (SSEs), such as those that frequently occur at the northern Hikurangi margin (HM) of New Zealand. To better understand fluid flow in the forearc system, we examined the relationship between elastic properties, compaction, porosity, and permeability of Cretaceous-to-Pliocene sedimentary rocks from the Raukumara peninsula. We found that the permeability of the deep wedge is too low to drain fluids, but fracturing increases permeability by orders of magnitude, making fracturing key for fluid flow. In weeks to months, plastic deformation and clay swelling heal the fractures, restoring the initial permeability. We conclude that overpressures at the northern HM might partly dissipate during SSEs due to enhanced permeability near faults. However, in the weeks to months following an SSE, healing in the prism will lower permeability, forcing pore pressure to rise and a new SSE to occur.

Plain Language Summary

Earth's crust is composed of many tectonic plates fitting together like jigsaw puzzle pieces. Tectonic plates subduct in the mantle along active converging margins, where the forces driving such a convergence can trigger large earthquakes. However, these subduction zones often deform without producing earthquakes, but through slow-slip. The Hikurangi Margin (HM) of New Zealand is a well-studied subduction zone, producing both earthquakes and slow-slip events. The northern HM exhibits more frequent and shallower slow-slip events than the southern margin. Understanding what controls such differences can help improve the general understanding of subduction zone fault mechanics and earthquakes. One of the hypotheses is that the differences between the deformation of the northern and southern HM are controlled by the pore pressure at depth. We tested the elastic and fluid-transport properties of four samples from the northern HM and found that the overriding plate, if not fractured, would be impermeable to fluids. We also tested a fractured sample and observed efficient healing that resets the initial permeability. We conclude that fracturing the overriding plate is fundamental to draining the fluids carried at depth by the subducting plate, and slow-slip events may create new pathways for fluids to escape to the seafloor.

1 Introduction

At the shallow (<15 km depth) portion of the plate interface of subduction zones, scientists have found that convergence between the tectonic plates is often accommodated by modes of slip in between fast earthquakes and aseismic creep (Saffer & Wallace, 2015). Slow-slip events (SSEs) represent one class of such transient phenomena, which can lead to several centimeters of slip over several days to months (Schwartz & Rokosky, 2007). The relatively large seismic moment released by shallow SSEs, comparable to that of earthquakes (Passarelli et al., 2021), proves the importance to understand SSEs and how they influence the seismogenic character of a convergent margin. Frictional properties and stress heterogeneities along the plate interface might favor SSEs (Barnes et al., 2020; Bell et al., 2010; Im et al., 2020; Rabinowitz et al., 2018). Subducting oceanic crust and sediments release large volumes of fluids (i.e., seawater and CO_2) whose pressure can exceed hydrostatic conditions when confined within low permeability rocks, lowering the effective stress on the shallow megathrust or splay faults and creating conditions conducive to SSEs (Kitajima & Saffer, 2012; Tsuji et al., 2008; Warren-Smith et al., 2019).

The northern Hikurangi margin (HM) of North Island, New Zealand, is a subduction zone with a shallow forearc and plate interface, where sediment accretion, compaction, and deformation have been modulated for millions of years by underthrusting seamounts (Gase et al., 2021; Sun et al., 2020). Subducting topography (e.g., seamounts) may cause stress heterogeneities (Bangs et al., 2023; Leah et al., 2022; Sun et al., 2020) and fluid pressure transients (Shaddox & Schwartz, 2019) that can lead to SSEs, several of which have been characterized in great detail by onshore geodetic and offshore absolute pressure gauge (APG) data (Yohler et al., 2019). Offshore Gisborne SSEs occur every 1-2 years and can last several weeks, during which 5 to 30 cm of slip may be accommodated (Wallace, 2020). Temporal variations in the character of earthquake focal mechanisms within the subducting oceanic crust provide compelling evidence for low effective stress before an SSE (Warren-Smith et al., 2019). This observation suggests that increases in fluid pressure enable SSEs and that the slip itself is accompanied by fluid release. Nevertheless, fluid transport through the accretionary wedge in this deformation cycle is not yet well understood (Antriasian et al., 2018).

The physical properties of accreted sediments of the northern HM and their relationship to slip phenomena have been studied recently with the use of cores and data from IODP expeditions (e.g., Wallace et al., 2019). The resulting studies have shed new light on the frictional properties, shallow dewatering, and faulting near the seafloor (Aretusini et al., 2021; Boulton et al., 2019, 2022; Dutilleul et al., 2021; Fagereng et al., 2019; French & Morgan, 2020; Shreedharan et al., 2022). However, to understand how fluid flow and deformation interplay in the deeper prism, we also must consider the physical properties of older, compacted, and diagenetically mature strata (Bland et al., 2015, Bassett et al., 2022). Here we present and discuss laboratory testing performed on rock samples from the subaerial northern HM as proxies of deep rocks in the prism to better understand fluid transport within the subduction zone.

2 Materials and Method

To test the compaction, elastic, and transport properties of rocks from the northern HM, we collected and performed experiments on outcrop samples from the Raukumara peninsula (Figs 1, S1) presenting different ages and degrees of diagenesis. In the central part of the peninsula, we collected a fine-grained sandstone from the Jurassic-to-Early Cretaceous Torlesse Supergroup forming the backstop for the accretionary wedge (sample MO02) (Adams & Graham, 1996; Mortimer et al., 2014). Just east of sample MO02 location, we sampled a calcareous fine-grained sandstone with a silty matrix from the Late Cretaceous-to-Paleocene Tinui Group (sample MT07) that likely represents an early passive margin deposit, now deeply buried in the accretionary wedge (Mortimer et al., 2014). Closer to the East coast, we collected a siltstone (sample GB13) from the middle Miocene Tolaga Group, which was deposited in slope basins after subduction initiated along the HM (van de Lagemaat et al., 2022), and a glauconitic fine-grained sandstone (sample FB12) from the Pliocene Mangaheia Group.

We determined mineral abundances and assemblages of each sample through X-ray diffraction (XRD) analyses and transmitted light microscopy by preparing 30 μm in thickness thin-sections. To estimate density, porosity, compressional and shear ultrasonic wave velocities (i.e., Vp and Vs), and helium gas permeability, we prepared cylindrical core plugs with parallel end faces for each sample. Samples were tested at the UT Austin Rock-Deformation-Laboratory for confining pressures (P_c) up to 200 MPa (~12.5 km depth for hydrostatic pore pressure and overburden density of 2.6 g/cm^3) and deviatoric vertical force (F_v) ~2.6 kN. Each core plug was mounted inside a PVC jacket and between two core holders equipped with ultrasonic transducers and fluid ports, which are used to saturate and measure the core permeability. This sample assembly is mounted inside the triaxial cell (NER Autolab 1500) between the load cell and the vertical force piston. We define the mean stress as $\sigma_M = \frac{\sigma_1+\sigma_2+\sigma_3}{3}$, where $\sigma_2 = \sigma_3 = P_c$ and σ_1 is the maximum vertical stress: $\sigma_1 = \sigma_d + P_c$, where $\sigma_d = \frac{F_V}{A}$ is the deviatoric stress, and A is the sectional area of the core plug. We also define effective stress (σ') as the difference between the mean stress and the pore pressure: $\sigma' = \sigma_M - P_p$.

We measured ultrasonic velocities using the transmission method at room temperature and a frequency of ~800 kHz (Birch, 1960). To understand the effect of saturation on Vp and Vs, we measured the ultrasonic velocities of sample GB13 saturated with water previously chemically equilibrated with the sample. During 30 hours, we recorded the injection of 4.7 ml of this fluid, equivalent to 136% of GB13 pore-space volume.

Sample permeabilities were calculated through the transient method measuring the pressure equilibration of the helium gas contained in two volumes connected to the sample end-faces and flowing through the sample (Sutherland & Cave, 1980). To understand the effect of porosity reduction on the permeability of young, loosely consolidated rocks, we measured FB12 permeability before and after mechanical compaction, which was assumed to be isotropic. First, we measured ultrasonic velocities and permeabilities at P_c up to 70 MPa and σ_d = 5 MPa, then, we increased P_c stepwise to 100, 150 and 200 MPa and waited for 19, 24 and 5 hours to measure creep until the observed shortening rate was less than 1 µm/hour. Finally, we measured the sample permeability for varying P_c up to 200 MPa.

To study how fractures influence the permeability of HM rocks, we split sample MT07 through a Brazilian test producing a sub-vertical fracture connecting the opposite end-faces of the core plug. Then, to study the effect of stress on permeability healing, we kept the sample dry and measured permeability as a function of σ' and we collected three micro-computed tomographies (µCT) to seek evidence of variations in fracture aperture. A detailed chronology of the operations follows: On day 1, after the Brazilian test, we collected µCT dataset S1. Between day 2 and 9 we performed the first permeability test (kT1) for σ' between 24 and 65 MPa. During kT1 (days 3 to 5) we promoted healing by keeping σ' to 65 MPa. After kT1 and for the next 39 days, the sample remained inside the pressure vessel at σ'~0 MPa. Between day 48 and day 77, we performed the second permeability test (kT2) at σ' ranging 5.6 to 64 MPa. At the end of kT2 we removed the sample from the pressure vessel and acquired µCT dataset S2. Then, the jacketed sample was placed inside a humidity-controlled chamber equipped with a water container and a thermo-hygrometer. For 72 hours, a medium to low vacuum (<0.5 bar) was maintained to promote water evaporation, causing the chamber relative humidity to remain above 97% and activating clays such as smectites with pronounced swelling properties (Villar et al., 2005). Finally, we acquired µCT dataset S3, and produced a thin section perpendicular to the sample axis. On the thin section, we examined the morphology of the fracture for evidence of clay infilling, possibly caused by plastic deformation and triggered by clay swelling.

Each µCT dataset comprises 1600, 33.3 µm resolution, 16-bits TIFF images perpendicular to the sample axis, recording the entire sample except 4.37 mm at the top and bottom. After normalization and segmentation, we calculated fracture apertures (B) for each CT dataset by producing fracture aperture distribution projections (FADP) whose mean and standard deviation provided average apertures (B_m) and associated uncertainties. We report more details on the methods in the supporting information.

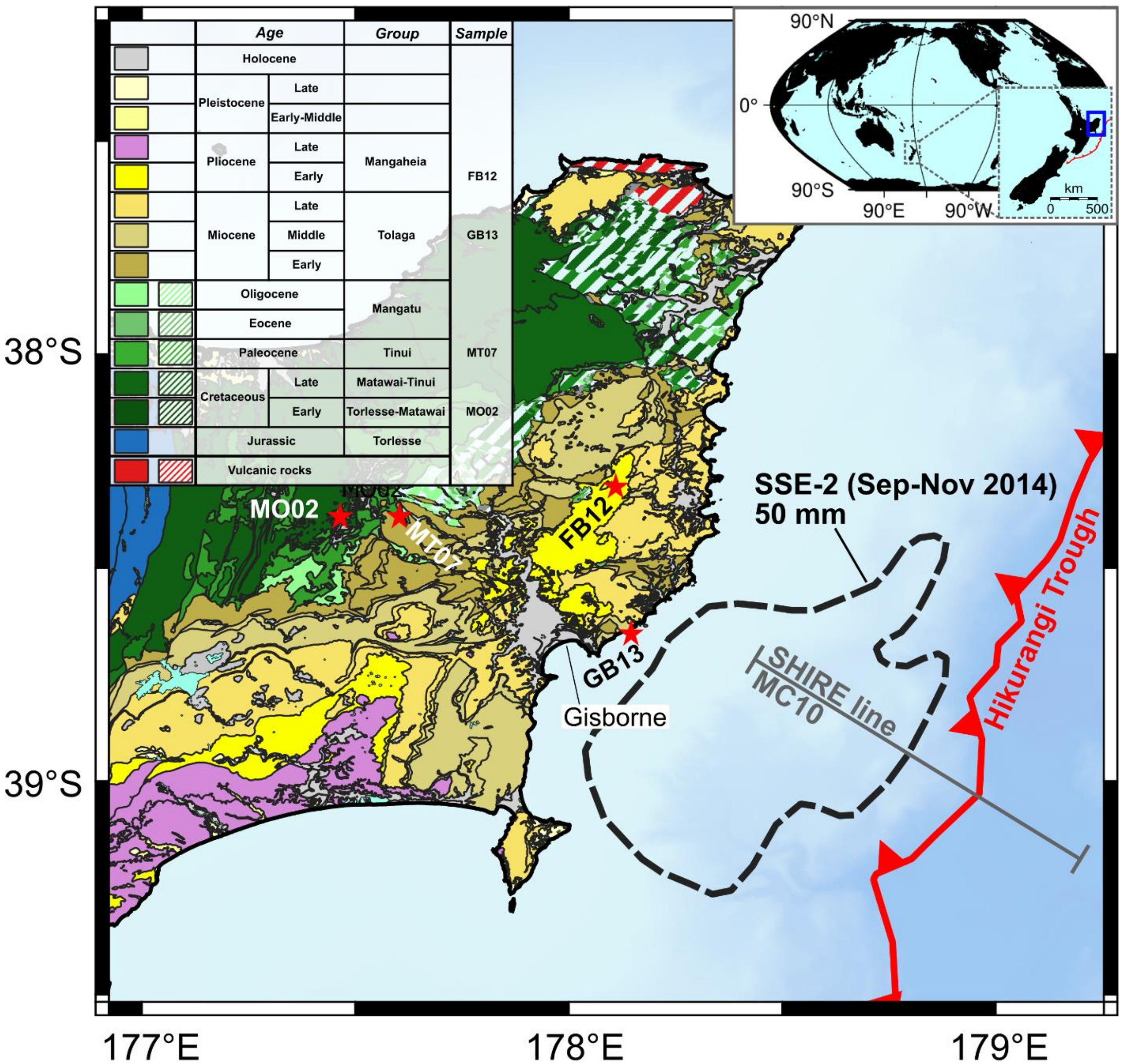

Figure 1. Geologic map of the Raukumara peninsula with the position of the rock samples used in this study (Mazengarb & Speden, 2000). The offshore dashed line contour marks the 50 mm geodetic slip model for the September-November 2014 SSE (Warren-Smith et al., 2019). The offshore line indicates the seismic line MC10 from the SHIRE project (Gase et al., 2021).

3 Results

The four samples (Fig S1) contain more than 35 wt% quartz and feldspars. The remaining minerals are calcite, and clays: chlorite, kaolinite, micas, illite, and smectite group minerals (Fig S2). Clays and swelling clays (i.e., illites and smectites) represent at least 24 wt% and 13 wt%, respectively (Fig S3). Porosities vary between 7 and 18%, where the tighter samples (MT07 and MO02) have a longer diagenetic or metamorphic history. Microphotography reveals that the grain size varies significantly among the four samples: Sample GB13 has the smallest grain size (<20 μm).

Ultrasonic velocity measurements (Fig 2A) show that Vp and Vs increase with σ_m, and the younger samples (FB12 and GB13) generally have lower wave speeds. Vp to Vs ratios vary between 1.6 and 1.95, with the least consolidated and youngest sample (FB12) exhibiting the highest values. After saturation, sample GB13 Vp increased by ~250 m/s on average while Vs decreased by ~100 m/s on average, increasing the Vp to Vs ratio from ~1.65 to ~1.95.

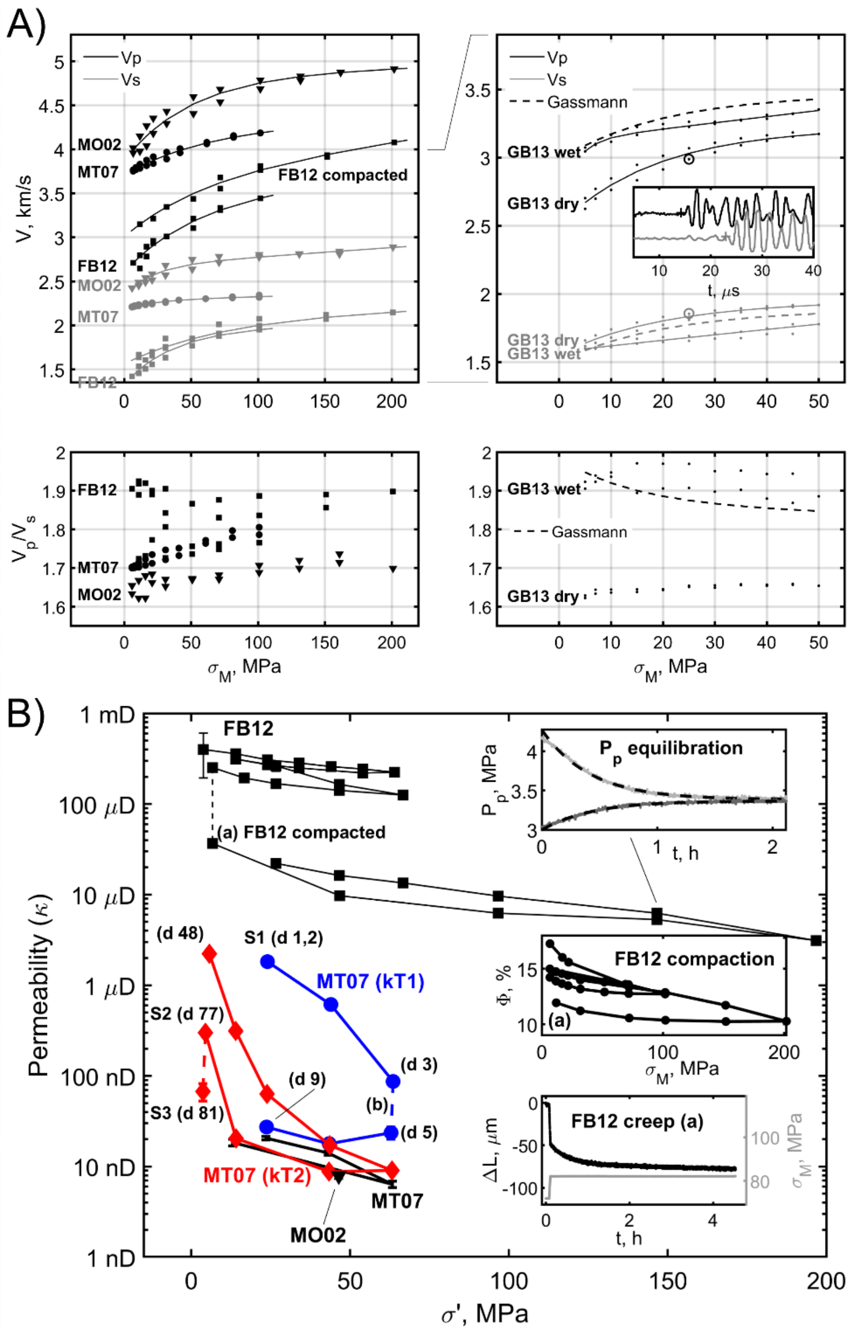

Figure 2. A) Left-top panel: ultrasonic velocities measured on the samples MO02, MT07 and FB12 as a function of σ_M. Right-top panel: ultrasonic Vp and Vs for sample GB13 when dry and saturated with water. Dashed lines indicate the theoretical saturated velocities from Gassmann fluid substitution (Gassmann, 1951). The inset shows examples of P and S waveforms recorded for the dry sample at the conditions indicated by the circled dots. Bottom panels: Vp to Vs ratios for the laboratory data and the fitting curves reported in the panels above. B) Permeabilities for samples FB12, MT07, and MO02 as a function of σ'. (a) "FB12 compaction" reports the loss of permeability due to the step-by-step increase of σ'; partial compaction and loss of porosity in sample FB12 are shown in "FB12 creep" and

"FB12 compaction" insets, respectively. "Pp equilibration" inset: example of pore pressure (Pp) equilibration and fitting curves (dashed lines). The blue and red curves show the permeability of the fractured sample MT07 during the two permability cycles (kT1 and kT2). (d X) near data points indicates X days since stage S1 (Fig 3A). Day 77 was the end of kT2 and stage S2 (Fig 3B): the sample was CT-scanned and exposed to a humid atmosphere for 72 hours. Day 81 was stage S3: we CT-scanned and remeasured the sample permeability (Fig 3C,D,E).

Before compaction, sample FB12 permeability ranged between 200 and 400 μD. Then, we raised P_c twice to 70 MPa, causing the permeability to decrease by a factor of two and porosity by 3% (i.e., at σ_m~7 MPa, porosity varied from 17.3 to 14.2%). In the following two cycles, where P_c reached 200 MPa, porosity decreased to 13.9%, and the permeability declined by almost an order of magnitude. Concurrently, the ultrasonic Vp increased from 2.6 km/s to 4 km/s.

Samples MO02 and MT07, when intact, have permeabilities below 100 nD, regardless of σ'. The permeability of the fractured MT07 evolved between stages S1, S2, and S3. After S1 and during the permeability cycle kT1, the permeability dropped from 2 μD to 87 nD. After exposing the sample to σ' ~65 MPa for more than 48 hours (Fig 4B b), we continued kT1 and found that the permeability further decreased to 24 nD. The permeability remained ~2 orders of magnitude lower than the initial permeability, i.e., around 30 nD, when σ' was reduced. After 39 days, the new increase of σ' during the second permeability cycle kT2, caused the permeability to drop to 9 nD. During the following decrease of σ', the permeability resembled pre-fracturing values. The last measurement of kT2 was performed at σ'=4.5 MPa and permeability was 300 nD, seven times lower than the initial value measured at σ'=5.6 MPa. After exposing the sample to humidity for 72 hours, the permeability, measured at σ'=3.7 MPa, decreased to 67 nD.

CT-scans visual inspection and analyses reveal the variation of B_m that varied from 190+/-110, to 72+/-43 and 84+/-45 µm during the stages S1, S2, and S3, respectively (Fig 3A,B,C). During the same stages, the number of voxels counted within the fracture varied respectively from ~934,000 to ~581,000 and ~797,000. Microphotography of sample MT07 at stage S3, shows that in several loci, the fracture collapsed, and a fine-grained amorphous mass infilled the fracture (Fig 3D,E). These observations suggest that varying confining pressure and humidification caused clay minerals plastic deformation and swelling, partially closing the fracture and reducing the permeability.

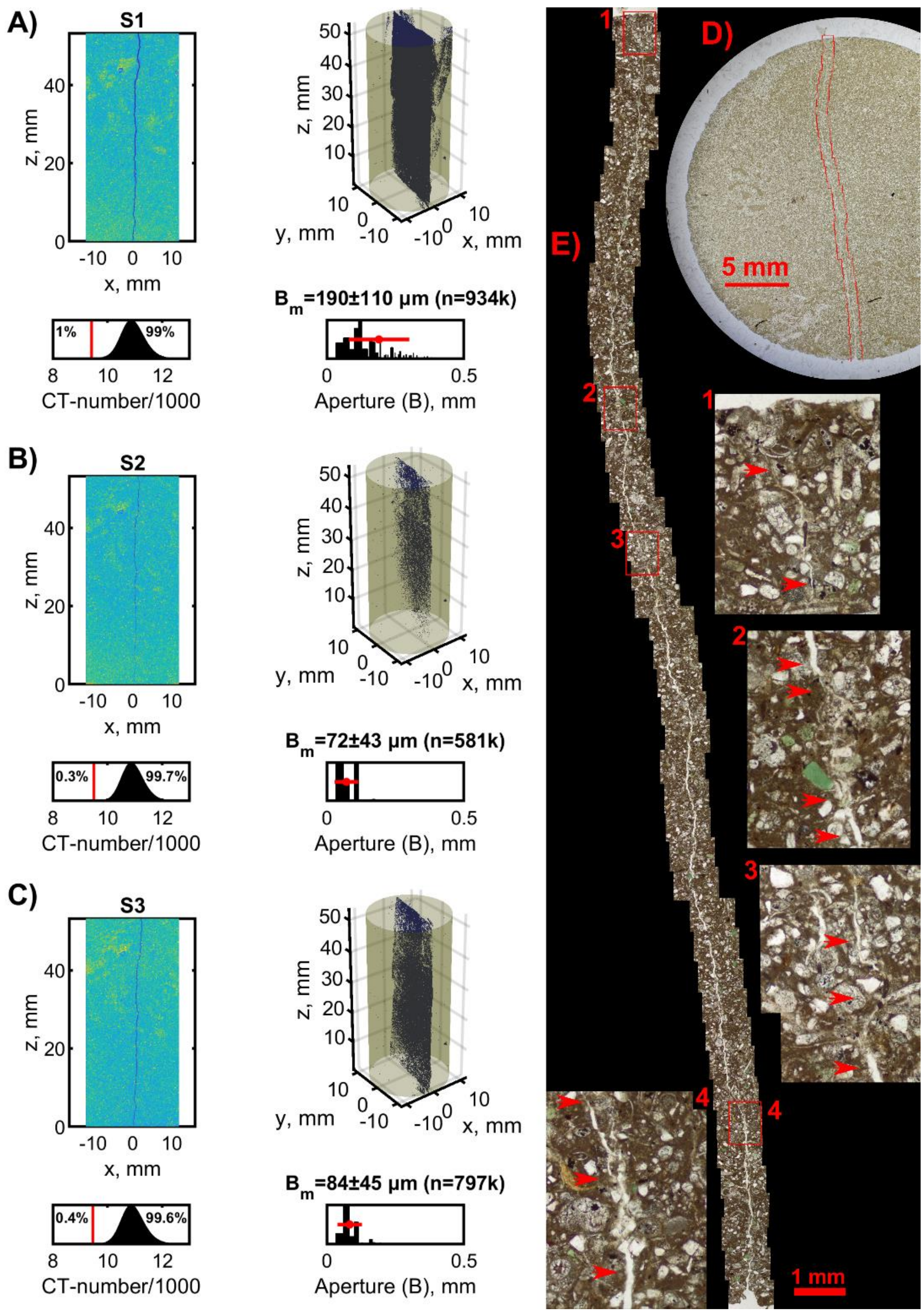

Figure 3. CT-scan and transmitted light microphotography of sample MT07 after fracturing. A, B, and C are CT-scans at stages S1, S2, and S3, respectively. Each top-left inset in these panels reports a section of the CT-scan model after normalization. CT-number distribution is shown in the bottom-left inset. The red vertical line indicates t_x (eq. S5). The percentages on the left and right of the red line indicate the relative quantity of voxels representing air and solid rock, respectively. The right top inset in each panel shows the binarized 3D model, where voxels collected within the fracture are blue. The bottom right inset show the aperture distribution (B), the calculated average and standard deviation (B_m and horizontal red bar), and the total count of voxel within the fracture (n). Panel D is a

microphotography of the thin section at stage S3. Panel E reports zooms from panel D. Insets 1 to 4 show fracture infill, which are highlighted by red arrows along with open fractures.

4 Discussion

We provide porosity-permeability relationships for rock samples from the subaerial northern HM under a range of confining pressures. Ultrasonic velocities of dry samples are similar to the seismic velocities estimated offshore New Zealand by the SHIRE project (Gase et al., 2021). The seismic reflectivity imaged along the transect MC10 shows the decollement along the prism base and several splay faults that may partly accommodate the convergence (Fig 4A). Inside the prism, Vp increases gradually from 2.0 km/s near the surface to 4.5 km/s at the prism base ~7 km below sea level. In Fig 4B, the comparison between the seismic and ultrasonic velocities suggests that sample FB12, and possibly also sample GB13, represent the modern slope basins on the outer prism, which is consistent with their depositional environment. The ultrasonic velocities of sample MT07 of the Tinui Group correspond well to the velocities of the deep part of the prism, where Vp reaches 4.5 km/s. Compaction and diagenesis must contribute to the increase of Vp with depth (Dvorkin & Nur, 1996; Saxena & Mavko, 2014). We measured an ultrasonic Vp of 4.8 km/s at 150 MPa in the Torlesse basement sample MO02, which is higher than what we imaged in the deep prism on Line MC10 (Fig 4), suggesting that there may not be a deep offshore portion of the Torlesse basement offshore northern HM (Bassett et al., 2022; Gase et al., 2021).

Our comparison between seismic and ultrasonic velocities in Figure 4 is semi-quantitative as uncertainty is introduced by microcracks produced during sample preparation – see SI for details (Eberhart-Phillips et al., 1989; Tsuji & Iturrino, 2008), and by frequency differences. Velocities in section MC10 and on our samples have been measured at frequencies around 20 Hz and 800 kHz, respectively. Considering the frequency range, a typical P-wave quality factor ranging from 30 to 150, and a nearly-constant Q model (Liu et al., 1976; Tisato et al., 2021), we should expect a velocity dispersion between 2.3 and 12%. Conversely, SHIRE and laboratory data were collected on saturated and dry samples, respectively. Saturation increases P-wave velocities of sample GB13 by 5 to 15%, suggesting that the effects of fluid saturation and anelasticity on velocities should counteract each other. Given the similarity in P-wave velocities and depositional environment, we suggest that the Tinui and Tolaga group rocks (samples MT07 and GB13) are good lithological proxies for the deep and shallow offshore Hikurangi prism, respectively.

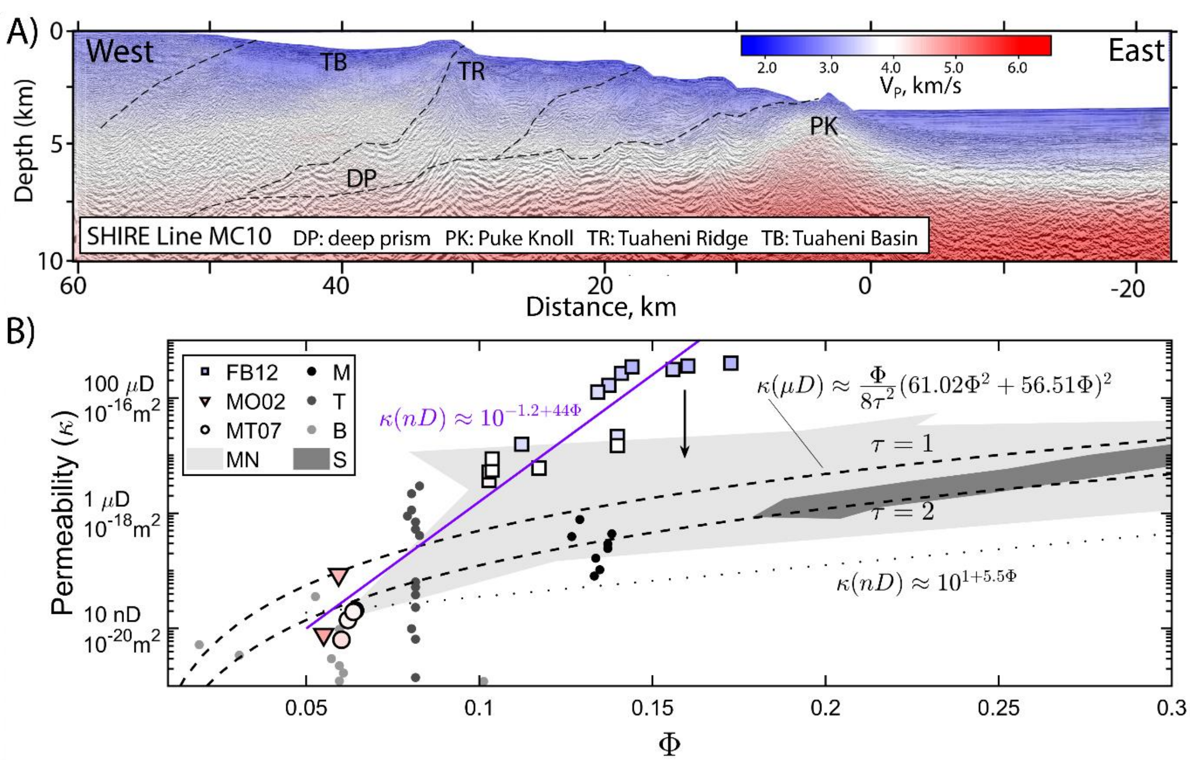

Figure 4. A) Velocity model along the SHIRE Line MC10 (Gase et al., 2021). B) Summary of laboratory result: permeabilities vs porosity and color-coded markers (colorbar in panel A) as a function of ultrasonic Vp for samples FB12, MO02, and MT07 (Tables S1 and S2). The arrow indicates in which direction the permeabilities vary when tests are performed using water rather than helium gas. Dashed lines indicate empirical permeability vs porosity according to eq. 3. The dotted line represents an average permeability for unconsolidated clays and possibly a lower bound for the permeability of HM sediments (Neuzil, 1994). S data (dark-gray area) are for siltstones (Reece et al., 2012). The continuous line fits our data and agrees with measured mudstone permeabilities indicated by the MN gray-shaded area (Magara, 1978; Neglia, 1979). Such a line also represents an upper bound for the permeability of HM rocks. M, T, and B data are permeabilities measured in boreholes: M by Reisdorf et al. (2016), Yu et al. (2017); T by Boisson et al. (2001); B by Intera Eng. Ltd. (2011), Roberts et al. (2011), Walsh (2011).

The permeability of our samples ranges from 1 nD to 1 mD, with the samples representing the deep part of the prism being the tightest. Neuzil (1994, 2019) compiled data from several studies on unconsolidated clays with a maximum porosity of 80%, and a few consolidated mudstone-siltstones with porosities (Φ) <35%. Saffer & Bekins (1998) followed Neuzil's work and described the permeability (κ) of the Nankai accretionary complex as:

$$\boldsymbol{\kappa(nD) \approx 10^{1+5.5\phi}} \qquad \text{eq. 1}$$

Equation 1 fits the porosity-permeability relationship of unconsolidated sediments and is a lower bound for the permeability of mudstones that are similar to our samples (Magara, 1978; Neglia, 1979; Reece et al., 2012). On the other hand, we found that:

$$\boldsymbol{\kappa(nD) \approx 10^{-1.2+44\phi}} \qquad \text{eq. 2}$$

fits our results and is an upper bound for the permeability of mudstones. We suggest that the permeabilities calculated from equations 1 and 2 (Fig 4B) overestimate permeabilities in the Northern Hikurangi accretionary prism at depths >1 km because helium gas is not as efficient as seawater in activating swelling clays whose expansion lowers the effective permeabilities (Villar et al., 2005); At burial depths >1-2 km, the porosity of clay-bearing sediments, mudstones, siltstone, and shales drops below 35% (Griffiths & Joshi, 1989; Magara, 1978; Skempton, 1969); Permeabilities measured in boreholes are typically orders of magnitude higher than those measured in the laboratory due to the presence of fractures (Fig 4B lines M,T,B) (Neuzil, 2019), and numerical models of permeability in microfractured claystones agree with the mudstone porosity-permeability in Fig 4B (Vora & Dugan, 2019). We also propose that the permeability of rocks in the Northern Hikurangi accretionary prism can be described by a Kozeny-Carman relation (dashed lines in Fig 4B):

$$\boldsymbol{\kappa = \frac{\phi}{8\tau^2} R^2} \qquad \text{eq. 3}$$

Where $\boldsymbol{\tau}$ is tortuosity, and *R* is the median pore diameter (Carman, 1997). We obtained $\boldsymbol{R(nm) = 61.02\phi^2 + 56.51\phi}$ from data reported by Hunt (1996) for similar lithologies.

Every 1-2 years, the northern HM experiences an SSE that lasts several weeks (Wallace, 2020). Recent analyses of the APG data offshore Gisborne have shown that the 2014 SSE may have experienced up to 30 cm of slip in the center of a ~100 km wide patch, though less displacement is expected along the edges (Yohler et al., 2019). Some authors have suggested that SSEs that originate along the decollement at the base of the wedge are accompanied by slip diverted to thrust faults in the Hikurangi accretionary wedge (Shaddox & Schwartz, 2019). We expect SSEs to deform and fracture the rocks along these thrust faults (Morgan et al., 2022). Our laboratory measurements before and after rock failure for sample MT07 show that the deeper prism, where Tinui Group equivalent rocks may be present, may experience large increases in permeability during an SSE.

In a few weeks, the fractured sample MT07 regained its pre-fracturing permeability. Between stages S1 and S2, the permeability recovery was achieved in dry conditions. Although sample MT07 and sample FB12 have different compaction levels and grain sizes, they share similar mineralogy. Thus, although limited, we expect plastic deformation also in sample MT07, likely concentrated near clays (Mondol et al., 2008). Between stages S2 and S3, the permeability decreased by a factor of 5 while B_m increased, suggesting clay expansion. Once confined, we expect that the hydrated clays would deform plastically, clogging the fracture more efficiently than dry clays and justifying the permeability loss. We propose that permeability healing is also present along HM faults, given the presence of clays at depth, especially above the 5-7 km deep temperature-controlled smectite-illite transition **(**Antriasian et al., 2018; Freed & Peacor, 1989; Pecher et al., 2017; Tisato & Marelli, 2013).

In the Hikurangi subduction zone, fluids expelled from pore space and fluids released by dehydration reactions travel along the plate interface or through the accretionary wedge (Ellis et al., 2015). As the fluid pressure increases near the decollement and inside the accretionary wedge, conditions may become favorable for an SSE (Burgreen-Chan et al., 2016; Kobayashi & Sato, 2021). Though this mechanism has been proposed for several subduction zones where SSE occur at larger depths (Audet et al., 2009; Kodaira et al., 2004), the analysis of Warren-Smith et al. (2019) on the northern HM, is also compatible with the sealing of fluid pathways after an SSE. The expansion and plastic deformation of clays may provide an efficient mechanism to reduce permeability over weeks or months after an SSE.

Permeability healing, favoring the development of overpressures, reconciles with the poor mechanical healing shown by Shreedharan et al. (2023), hindering elastic energy accumulation, because both set conditions conducive to SSEs.

5 Conclusions

We provided relationships between porosity, permeability, and confining pressure for rocks that make up the accretionary prism of the northern HM. We suggest an empirical porosity-permeability relationship to model fluid transport and estimate effective stress in shallow subduction zones. Mechanical failure of these rocks enhances permeability, but over the course of several weeks, healing reduces the permeability again, suggesting that after an SSE, sediments deep in the northern HM accretionary prism can recover permeability efficiently within the time frame of an SSE as a mechanism explaining the regular recurrence of these events.

Acknowledgments

We thank Lucy Flesh, Carolyn Boulton, and one anonymous reviewer for the insightful reviews, Luc Lavier and Dominic Strogen for the valuable discussions. NSF supported this research (grant OCE-1949171).

Open Research

Data are publicly available upon publication at https://doi.org/10.18738/T8/RMXMIQ or can be requested to the corresponding author.

References

Adams, C. J., & Graham, I. J. (1996). Metamorphic and tectonic geochronology of the Torlesse Terrane, Wellington, New Zealand. *New Zealand Journal of Geology and Geophysics*, *39*(2), 157–180. https://doi.org/10.1080/00288306.1996.9514703

Antriasian, A., Harris, R. N., Tréhu, A. M., Henrys, S. A., Phrampus, B. J., Lauer, R., et al. (2018). Thermal Regime of the Northern Hikurangi Margin, New Zealand. *Geophysical Journal International*. https://doi.org/10.1093/gji/ggy450

Aretusini, S., Meneghini, F., Spagnuolo, E., Harbord, C. W., & Di Toro, G. (2021). Fluid pressurisation and earthquake propagation in the Hikurangi subduction zone. *Nature Communications*, *12*(1), 2481. https://doi.org/10.1038/s41467-021-22805-w

Audet, P., Bostock, M. G., Christensen, N. I., & Peacock, S. M. (2009). Seismic evidence for overpressured subducted oceanic crust and megathrust fault sealing. *Nature*, *457*, 76–78. https://doi.org/10.1038/nature07650

Bangs, N. L., Morgan, J. K., Bell, R. E., Han, S., Arai, R., Gase, A. C., et al. (2023). Slow slip along the Hikurangi margin linked to fluid-rich sediments trailing subducting seamounts. *Nature Geoscience*, *IN PRESS*.

Barnes, P. M., Wallace, L. M., Saffer, D. M., Bell, R. E., Underwood, M. B., Fagereng, A., et al. (2020). Slow slip source characterized by lithological and geometric heterogeneity. *Science Advances*, *6*(13). https://doi.org/10.1126/sciadv.aay3314

Bassett, D., Arnulf, A., Henrys, S., Barker, D., Avendonk, H., Bangs, N., et al. (2022). Crustal Structure of the Hikurangi Margin From SHIRE Seismic Data and the Relationship Between Forearc Structure and Shallow Megathrust Slip Behavior. *Geophysical Research Letters*, *49*(2). https://doi.org/10.1029/2021GL096960

Bell, R., Sutherland, R., Barker, D. H. N., Henrys, S., Bannister, S., Wallace, L., & Beavan, J. (2010). Seismic reflection character of the Hikurangi subduction interface, New Zealand, in the region of repeated Gisborne slow slip events. *GJI*, *180*, 34–48. https://doi.org/10.1111/j.1365-246X.2009.04401.x

Birch, F. (1960). The velocity of compressional waves in rocks to 10 kilobars: 1. *Journal of Geophysical Research*, *65*(4), 1083–1102. https://doi.org/10.1029/JZ065i004p01083

Bland, K. J., Uruski, C. I., & Isaac, M. J. (2015). Pegasus Basin, eastern New Zealand: A stratigraphic record of subsidence and subduction, ancient and modern. *NZJGG*, *58*, 319–343. https://doi.org/10.1080/00288306.2015.1076862

Boisson, J.-Y., Bertrand, L., Heitz, J.-F., & Golvan, Y. (2001). In situ and laboratory investigations of fluid flow through an argillaceous formation at different scales of space and time, Tournemire tunnel, southern France. *Hydrogeology Journal*, *9*(1), 108–123. https://doi.org/10.1007/s100400000119

Boulton, C., Niemeijer, A. R., Hollis, C. J., Townend, J., Raven, M. D., Kulhanek, D. K., & Shepherd, C. L. (2019). Temperature-dependent frictional properties of heterogeneous Hikurangi Subduction Zone input sediments, ODP Site 1124. *Tectonophysics*, *757*, 123–139. https://doi.org/10.1016/j.tecto.2019.02.006

Boulton, C., Mizera, M., Niemeijer, A. R., Little, T. A., Müller, I. A., Ziegler, M., & Hamers, M. F. (2022). Observational and theoretical evidence for frictional-viscous flow at shallow crustal levels. *Lithos*, *428–429*, 106831. https://doi.org/10.1016/j.lithos.2022.106831

Burgreen-Chan, B., Meisling, K. E., & Graham, S. (2016). Basin and petroleum system modelling of the East Coast Basin, New Zealand: a test of overpressure scenarios in a convergent margin. *Basin Research*, *28*(4), 536–567. https://doi.org/10.1111/bre.12121

Carman, P. C. (1997). Fluid flow through granular beds. *Chemical Engineering Research and Design*, *75*, S32–S48. https://doi.org/10.1016/S0263-8762(97)80003-2

Dutilleul, J., Bourlange, S., & Géraud, Y. (2021). Porosity and compaction state at the active Pāpaku thrust fault in the frontal accretionary wedge of the north Hikurangi margin. *G3*, *22*, e2020GC009325. https://doi.org/10.1029/2020GC009325

Dvorkin, J., & Nur, A. (1996). Elasticity of high-porosity sandstones: Theory for two North Sea data sets. *GEOPHYSICS*, *61*(5), 1363–1370. https://doi.org/10.1190/1.1444059

Eberhart-Phillips, D., Han, D.-H., & Zoback, M. D. (1989). Empirical relationships among seismic velocity, effective pressure, porosity, and clay content in sandstone. *GEOPHYSICS*, *54*(1), 82–89. https://doi.org/10.1190/1.1442580

Ellis, S., Fagereng, Å., Barker, D., Henrys, S., Saffer, D., Wallace, L., et al. (2015). Fluid budgets along the northern Hikurangi subduction margin, New Zealand: the effect of a subducting seamount on fluid pressure. *GJI*, *202*, 277–297. https://doi.org/10.1093/gji/ggv127

Fagereng, Å., Savage, H. M., Morgan, J. K., Wang, M., Meneghini, F., Barnes, P. M., et al. (2019). Mixed deformation styles observed on a shallow subduction thrust, Hikurangi margin, New Zealand. *Geology*, *47*, 872–876. https://doi.org/10.1130/G46367.1

Freed, R. L., & Peacor, D. R. (1989). Variability in temperature of the smectite/illite reaction in Gulf Coast sediments. *Clay Minerals*, *24*(2), 171–180. https://doi.org/10.1180/claymin.1989.024.2.05

French, M. E., & Morgan, J. K. (2020). Pore Fluid Pressures and Strength Contrasts Maintain Frontal Fault Activity, Northern Hikurangi Margin, New Zealand. *GRL*, *47*, e2020GL089209. https://doi.org/10.1029/2020GL089209

Gase, A. C., Van Avendonk, H. J. A., Bangs, N. L., Bassett, D., Henrys, S. A., Barker, D. H. N., et al. (2021). Crustal Structure of the Northern Hikurangi Margin, New Zealand: Variable Accretion and Overthrusting Plate Strength Influenced by Rough Subduction. *Journal of Geophysical Research: Solid Earth*, *126*(5), e2020JB021176. https://doi.org/10.1029/2020JB021176

Gassmann, F. (1951). Elastic waves through a packing of spheres. *GEOPHYSICS*, *16*(4), 673–685. https://doi.org/10.1190/1.1437718

Griffiths, F. J., & Joshi, R. C. (1989). Change in pore size distribution due to consolidation of clays. *Géotechnique*, *39*(1), 159–167. https://doi.org/10.1680/geot.1989.39.1.159

Hunt, J. M. (1996). *Petroleum geochemistry and geology* (2nd ed). New York: W.H. Freeman.

Im, K., Saffer, D., Marone, C., & Avouac, J. P. (2020). Slip-rate-dependent friction as a universal mechanism for slow slip events. *Nature Geoscience*, *13*(10). https://doi.org/10.1038/s41561-020-0627-9

Intera Eng. Ltd. (2011). *Descriptive Geosphere Site Model*. 2011: Intera Eng. Ltd.

Kitajima, H., & Saffer, D. M. (2012). Elevated pore pressure and anomalously low stress in regions of low frequency earthquakes along the Nankai Trough subduction megathrust: LOW STRESS AT LOW SEISMIC VELOCITY ZONE. *Geophysical Research Letters*, *39*(23), n/a-n/a. https://doi.org/10.1029/2012GL053793

Kobayashi, T., & Sato, T. (2021). Estimating Effective Normal Stress During Slow Slip Events From Slip Velocities and Shear Stress Variations. *Geophysical Research Letters*, *48*(20). https://doi.org/10.1029/2021GL095690

Kodaira, S., Iidaka, T., Kato, A., Park, J.-O., Iwasaki, T., & Kaneda, Y. (2004). High pore fluid pressure may cause silent slip in the Nankai Trough. *Science*, *304*, 1295–1298.

van de Lagemaat, S. H. A., Mering, J. A., & Kamp, P. J. J. (2022). Geochemistry of syntectonic carbonate veins within Late Cretaceous turbidites, Hikurangi margin (New Zealand): Implications for a mid-Oligocene age of subduction initiation. *G3*, *23*, e2021GC010125. https://doi.org/10.1029/2021GC010125

Leah, H., Fagereng, Å., Bastow, I., Bell, R., Lane, V., Henrys, S., et al. (2022). The northern Hikurangi margin three-dimensional plate interface in New Zealand remains rough 100 km from the trench. *Geology*, *50*, 1256–1260. https://doi.org/10.1130/G50272.1

Liu, H.-P., Anderson, D. L., & Kanamori, H. (1976). Velocity dispersion due to anelasticity; implications for seismology and mantle composition. *Geophysical Journal International*, *47*(1), 41–58. https://doi.org/10.1111/j.1365-246X.1976.tb01261.x

Magara, K. (1978). *Compaction and fluid migration: practical petroleum geology*. Amsterdam, New York: Elsevier Scientific Pub. Co. ; Distributors for the U.S. and Can., Elsevier North-Holland.

Mazengarb, C., & Speden, I. G. (2000). Geology of the Raukumara area. geological map 6 60 p. + 1 fold. map, Lower Hutt: Institute of Geological & Nuclear Sciences.

Mondol, N. H., Bjørlykke, K., & Jahren, J. (2008). Experimental compaction of clays: relationship between permeability and petrophysical properties in mudstones. *Petroleum Geoscience*, *14*(4), 319–337. https://doi.org/10.1144/1354-079308-773

Morgan, J. K., Solomon, E. A., Fagereng, A., Savage, H. M., Wang, M., Meneghini, F., et al. (2022). Seafloor overthrusting causes ductile fault deformation and fault sealing along the Northern Hikurangi Margin. *Earth and Planetary Science Letters*, *593*, 117651. https://doi.org/10.1016/j.epsl.2022.117651

Mortimer, N., Rattenbury, M., King, P., Bland, K., Barrell, D., Bache, F., et al. (2014). High-level stratigraphic scheme for New Zealand rocks. *New Zealand Journal of Geology and Geophysics*, *57*(4), 402–419. https://doi.org/10.1080/00288306.2014.946062

Neglia, S. (1979). Migration of Fluids in Sedimentary Basins1. *AAPG Bulletin*, *63*(4), 573–597. https://doi.org/10.1306/2F918194-16CE-11D7-8645000102C1865D

Neuzil, C. E. (1994). How permeable are clays and shales? *Water Resources Research*, *30*(2), 145–150. https://doi.org/10.1029/93WR02930

Neuzil, C. E. (2019). Permeability of Clays and Shales. *Annual Review of Earth and Planetary Sciences*, *47*(1), 247–273. https://doi.org/10.1146/annurev-earth-053018-060437

Passarelli, L., Selvadurai, P. A., Rivalta, E., & Jónsson, S. (2021). The source scaling and seismic productivity of slow slip transients. *Science Advances*, *7*(32), eabg9718. https://doi.org/10.1126/sciadv.abg9718

Pecher, I. A., Villinger, H., Kaul, N., Crutchley, G. J., Mountjoy, J. J., Huhn, K., et al. (2017). A Fluid Pulse on the Hikurangi Subduction Margin: Evidence From a Heat Flux Transect Across the Upper Limit of Gas Hydrate Stability. *Geophysical Research Letters*, *44*(24). https://doi.org/10.1002/2017GL076368

Rabinowitz, H. S., Savage, H. M., Skarbek, R. M., Ikari, M. J., Carpenter, B. M., & Collettini, C. (2018). Frictional behavior of input sediments to the Hikurangi trench, New Zealand. *G3*, *19*, 2973–2990. https://doi.org/10.1029/2018GC007633

Reece, J. S., Flemings, P. B., Dugan, B., Long, H., & Germaine, J. T. (2012). Permeability-porosity relationships of shallow mudstones in the Ursa Basin, northern deepwater Gulf of Mexico: MUDSTONE PERMEABILITY-POROSITY BEHAVIOR. *Journal of Geophysical Research: Solid Earth*, *117*(B12), n/a-n/a. https://doi.org/10.1029/2012JB009438

Reisdorf, A. G., Hostettler, B., Jaeggi, D., Deplazes, G., Blaesi, H., Morard, A., et al. (2016). Litho- and biostratigraphy of the 250 m-deep Mont Terri BDB-1 borehole through the Opalinus Clay and bounding formations, St Ursanne, Switzerland. https://doi.org/10.13140/RG.2.2.15045.04322

Roberts, R., Chace, D., Beauheim, R., & Avis, J. (2011). *Analysis of straddle-packer tests in DGR boreholes* (Technical report No. TR-08-32). Ottawa, Canada: Geofirma Eng. Ltd.

Saffer, D. M., & Bekins, B. A. (1998). Episodic fluid flow in the Nankai accretionary complex: Timescale, geochemistry, flow rates, and fluid budget. *Journal of Geophysical Research: Solid Earth*, *103*(B12), 30351–30370. https://doi.org/10.1029/98JB01983

Saffer, D. M., & Wallace, L. M. (2015). The frictional, hydrologic, metamorphic and thermal habitat of shallow slow earthquakes. *NG*, *8*, 594–600. https://doi.org/10.1038/ngeo2490

Saxena, N., & Mavko, G. (2014). Exact equations for fluid and solid substitution. *GEOPHYSICS*, *79*(3), L21–L32. https://doi.org/10.1190/geo2013-0187.1

Schwartz, S. Y., & Rokosky, J. M. (2007). Slow slip events and seismic tremor at circum-Pacific subduction zones. *RG*, *45*, RG3004. https://doi.org/10.1029/2006RG000208

Shaddox, H. R., & Schwartz, S. Y. (2019). Subducted seamount diverts shallow slow slip to the forearc of the northern Hikurangi subduction zone, New Zealand. *Geology*, *47*, 415–418. https://doi.org/10.1130/G45810.1

Shreedharan, S., Ikari, M., Wood, C., Saffer, D., Wallace, L., & Marone, C. (2022). Frictional and Lithological Controls on Shallow Slow Slip at the Northern Hikurangi Margin. *G3*, *23*, e2021GC010107. https://doi.org/10.1029/2021GC010107

Shreedharan, S., Saffer, D., Wallace, L. M., & Williams, C. (2023). Ultralow frictional healing explains recurring slow slip events. *Science*, *379*(6633), 712–717. https://doi.org/10.1126/science.adf4930

Skempton, A. W. (1969). The consolidation of clays by gravitational compaction. *Quarterly Journal of the Geological Society*, *125*(1–4), 373–411. https://doi.org/10.1144/gsjgs.125.1.0373

Sun, T., Saffer, D., & Ellis, S. (2020). Mechanical and hydrological effects of seamount subduction on megathrust stress and slip. *Nature Geoscience*, *13*(3), 249–255. https://doi.org/10.1038/s41561-020-0542-0

Sutherland, H. J., & Cave, S. P. (1980). Argon gas permeability of new mexico rock salt under hydrostatic compression. *International Journal of Rock Mechanics and Mining Sciences & Geomechanics Abstracts*, *17*(5), 281–288. https://doi.org/10.1016/0148-9062(80)90810-4

Tisato, N., & Marelli, S. (2013). Laboratory measurements of the longitudinal and transverse wave velocities of compacted bentonite as a function of water content, temperature, and confining pressure: ELASTIC PROPERTIES OF BENTONITE. *Journal of Geophysical Research: Solid Earth*, *118*(7), 3380–3393. https://doi.org/10.1002/jgrb.50252

Tisato, N., Madonna, C., & Saenger, E. H. (2021). Attenuation of Seismic Waves in Partially Saturated Berea Sandstone as a Function of Frequency and Confining Pressure. *Frontiers in Earth Science*, *9*, 641177. https://doi.org/10.3389/feart.2021.641177

Tsuji, T., & Iturrino, G. J. (2008). Velocity-porosity relationships in oceanic basalt from eastern flank of the Juan de Fuca Ridge: The effect of crack closure on seismic velocity. *Exploration Geophysics*, *39*(1), 41–51. https://doi.org/10.1071/EG08001

Tsuji, T., Tokuyama, H., Costa Pisani, P., & Moore, G. (2008). Effective stress and pore pressure in the Nankai accretionary prism off the Muroto Peninsula, southwestern Japan. *Journal of Geophysical Research*, *113*(B11), B11401. https://doi.org/10.1029/2007JB005002

Villar, M. V., Martín, P. L., & Barcala, J. M. (2005). Modification of physical, mechanical and hydraulic properties of bentonite by thermo-hydraulic gradients. *Engineering Geology*, *81*(3), 284–297. https://doi.org/10.1016/j.enggeo.2005.06.012

Vora, H. B., & Dugan, B. (2019). Porosity-Permeability Relationships in Mudstone from Pore-Scale Fluid Flow Simulations using the Lattice Boltzmann Method. *Water Resources Research*, *55*(8), 7060–7071. https://doi.org/10.1029/2019WR024985

Wallace, Laura M. (2020). Slow Slip Events in New Zealand. *AREPS*, *48*, 175–203. https://doi.org/10.1146/annurev-earth-0717190055104

Wallace, L.M., Saffer, D. M., Barnes, P. M., Pecher, I. A., Petronotis, K. E., LeVay, L. J., & the Expedition 372/375 Scientists. (2019). *Hikurangi Subduction Margin Coring, Logging, and Observatories*. College Station, TX: Proceedings of the International Ocean Discovery Program, 372B/375. https://doi.org/10.14379/iodp.proc.372B375.102.2019

Walsh, R. (2011). *Compilation and consolidation of field and laboratory data for hydrogeological properties* (DGR Site Charact. Doc. No. TR-08-10). Ottawa, Canada: Geofirma Eng. Ltd.

Warren-Smith, E., Fry, B., Wallace, L., Chon, E., Henrys, S., Sheehan, A., et al. (2019). Episodic stress and fluid pressure cycling in subducting oceanic crust during slow slip. *Nature Geoscience*, *12*(6), 475–481. https://doi.org/10.1038/s41561-019-0367-x

Yohler, R., Bartlow, N., Wallace, L. M., & Williams, C. (2019). Time-Dependent Behavior of a Near-Trench Slow-Slip Event at the Hikurangi Subduction Zone. *Geochemistry, Geophysics*, *Geosystems*, *20*(8), 4292–4304. https://doi.org/10.1029/2019GC008229

Yu, C., Matray, J.-M., Gonçalvès, J., Jaeggi, D., Gräsle, W., Wieczorek, K., et al. (2017). Comparative study of methods to estimate hydraulic parameters in the hydraulically undisturbed Opalinus Clay (Switzerland). *Swiss Journal of Geosciences*, *110*(1), 85–104. https://doi.org/10.1007/s00015-016-0257-9